Flow Over a Step Cylinder using Partially-Averaged Navier-Stokes Equations with Application Towards Subsea Power Cables

U Shaukat [1,*], A Schnepf [1,2] and K E T Giljarhus [1]

[1] University of Stavanger, Department of Mechanical and Structural Engineering and Materials Science, Stavanger, Norway
[2] CoreMarine AS, Stavanger, Norway

E-mail: `usman.shaukat@uis.no`

Abstract. Understanding the flow characteristics of buoyancy sections in power cable and umbilical configurations is crucial for analyzing floating offshore wind turbine systems. Buoyancy sections decouple the motions from the floater and the destination point to ensure the integrity of the system. Using accurate drag coefficients in their design is essential, as they significantly impact the overall behavior of the configuration. Therefore, Computational Fluid Dynamic (CFD) analysis is performed in the present study on a single buoyancy module attached to a power cable represented by a step cylinder configuration. The Partially-Averaged Navier-Stokes (PANS) turbulence model is applied. Its accuracy is validated against experimental findings of a wall-mounted cantilever cylinder and an infinite cylinder. The numerical results reveal that the larger diameter cylinder (LDC) section reduces the drag experienced by the smaller diameter cylinder (SDC) section near the junction. The LDC has a sharp, chamfered, and filleted edge replicating the various shapes of buoyancy modules. The edge design of the LDC affects the drag forces and flow patterns. The SDC has an 8 % lower drag coefficient in the fillet edge case than the sharp edge case. The drag coefficient is 3.5 % lower for the LDC in the filleted edge case than the sharp edge case. The sharp edge causes a significant separation of the fluid upstream of the SDC. However, this separation is notably reduced when the LDC has a chamfered or filleted edge. Detailed drag coefficients for buoyancy section analysis of power cable configurations have been deduced from the presented results.

1. Introduction

Power cables transmit electrical energy generated by offshore wind turbines to consumers, whether on land or at sea, such as oil and gas platforms. In the case of floating offshore wind turbines, the power cable configurations have dynamic sections where the cable is designed to float freely in the water from its hang-off location to the seabed or the next floater. They are installed in specific configurations to maintain safe operation and prevent excessive loading. These configurations often require buoyancy modules attached to the power cable at certain sections to keep its shape and to decouple the motions from the floating offshore wind turbine to the next connection point.

Besides their use in offshore wind technologies, buoyancy modules have been applied in umbilical and riser configurations within the oil and gas industry. The recommended practice DNV-RP-C205 [1] specifically addresses risers equipped with buoyancy elements and provides

guidance on their analysis. While the tangential drag coefficients are determined based on the experimental findings of Huse and Erling [2], DNV-RP-C205 recommends estimating the drag coefficients in transverse (normal) direction on an infinite cylinder. Drag coefficients for buoyancy modules are estimated by multiplying the infinite cylinder drag coefficient with a reduction factor according to the finite length. Selecting the appropriate transverse coefficient can have a substantial influence on the behavior of the system. The Morison equation is often applied in common software used for the hydrodynamic analysis of offshore systems. Therefore, when a current flows in the transverse direction towards the power cable, umbilical, or riser, it encounters a much larger resistance area than in the tangential direction. This can result in notable differences in simulation results when employing various values obtained from different methods to estimate the drag coefficient. For example, Schnepf et al. [3] observed a difference of about 8% in power cable tensions when using infinitely and finitely long cylinder approaches to determine the drag coefficient.

Due to the symmetric characteristic of the system, the focus can be on the specific region where a buoyancy module interfaces with the power cable. Therefore, for simplicity, this configuration can be replicated by a step cylinder. A step cylinder comprises a large diameter cylinder (LDC) and a small diameter cylinder (SDC) section merged together. Moreover, numerical and experimental studies on step cylinders were performed either at low Reynolds numbers with importance to flow structures [4, 5, 6] or on the high diameter ratio of the step cylinder [7].

The present study investigates transverse forces acting along smooth cylinders at higher Reynolds number flows in the subcritical regime. Different cylinder configurations are investigated, including infinite and finite cylinders and step cylinders with sharp, chamfered, and filleted edges.

2. Methodology and numerical setup

A smooth step cylinder is investigated in the present study, focusing on forces and changes in the flow pattern due to the diameter change between the LDC and SDC. In offshore systems, the Reynolds number can vary from laminar to supercritical depending on the diameter of the cylinders and the current speed. For this study, the focus is specifically on Reynolds numbers in the subcritical regime because the power cable configurations are commonly designed below the critical regime. Therefore, the LDC and SDC sections have Reynolds numbers of 2.5×10^4 and 6250, respectively, which fall in the subcritical range. The flow is initially laminar at these Reynolds numbers, separating and transitioning to turbulence along the free shear layer around the cylinder [8]. The present study also investigates changes in the overall flow patterns and sectional drag forces due to chamfering and filleting of the edges of the LDC because practically the edges of buoyancy modules are usually not sharp; see [9].

Simulation results are presented using a scale-resolved turbulence model, in which large-scale eddies are resolved while small-scale eddies are modeled. These models have shown improved prediction in bluff body aerodynamics. This study applies the Partially-Averaged Navier-Stokes (PANS) equation model first developed by Girimaji [10]. The k ω SST PANS model is implemented in OpenFOAM v2206 and chosen for the study due to improved near-wall boundary layer modeling [11].

PANS switches between direct numerical simulation (DNS) and solving Unsteady Reynolds-Averaged Navier-Stokes (URANS) equations with the help of the blending factor f_k. This factor represents the resolved-to-unresolved turbulence ratio in the PANS equations [12]. The value of f_k ranges between 0 and 1, where 0 means DNS and 1 means URANS are applied.

Since PANS simulations are sensitive to the f_k parameter, many research methodologies have been established to dynamically adjust f_k value across the domain [12, 13, 14]. There is considerable uncertainty involved in the process of selecting an ideal dynamic formulation

of f_k that can be universally applied to all cases. Moreover, Klapwijk et al. [15] argued that the current dynamic f_k approaches are not satisfactory with its sensitivity to grid resolution and suggested that the constant f_k approach is still a better way to apply PANS for industrial applications. Therefore, this study chooses a discrete constant f_k, and a validation study with two f_k values is initially performed for the benchmark case of a cantilever wall-mounted cylinder. The value that produces better flow predictions is chosen for the step cylinder study.

2.1. Numerical settings

SnappyHexMesh utility is used to generate mesh consisting of hexahedra, polyhedra, and prisms. A refinement level of four is applied at and near the cylinder surface, and a uniform boundary layer is generated close to the cylinder to resolve the viscous sublayer along the whole cylinder, as shown in Figure 2. Therefore, the average y^+, which is the nondimensional distance from the wall to the first grid point, approached a value of one near the wall of the cylinder. The spatial discretization relies on a second-order Linear-Upwind Stabilized Transport (LUST) scheme, which combines a 75 % linear weight to enhance accuracy and a 25 % linear upwind weight for stabilization. Concurrently, a second-order backward scheme is employed for temporal discretization. Throughout the simulation, temporal discretization is such that the maximum Courant Number for all time steps is smaller than one. Pressure and velocity equations are solved using the Pressure-Implicit with Splitting of Operators (PISO) algorithm.

2.1.1. Cantilever finite cylinder model validation setup

In this study, the simulation setup reproduces the wind tunnel setup illustrated in Figure 1. The cylinder diameter of $D = 0.03 \, \text{m}$ and inlet velocity of $10 \, \text{m/s}$ generated a Reynolds number of approximately 2×10^4. The test section measures $24D \times 24D \times 20D$ ($L \times W \times H$) in three dimensions. The cylinder has a height of $6D$, resulting in a blockage ratio of $1.2 \, \%$. Slip boundary conditions are applied at the top and lateral patch. No slip conditions are applied to the cylinder and bottom patch. Uniform fixed inlet velocity is applied to the inlet patch. As a first step, a precursor RANS simulation is run up to 200 iterations, followed by an unsteady PANS simulation for $1.336 \, \text{s}$ for up to 445 vortex-shedding cycles. The fields were averaged after 112 vortex-shedding cycles.
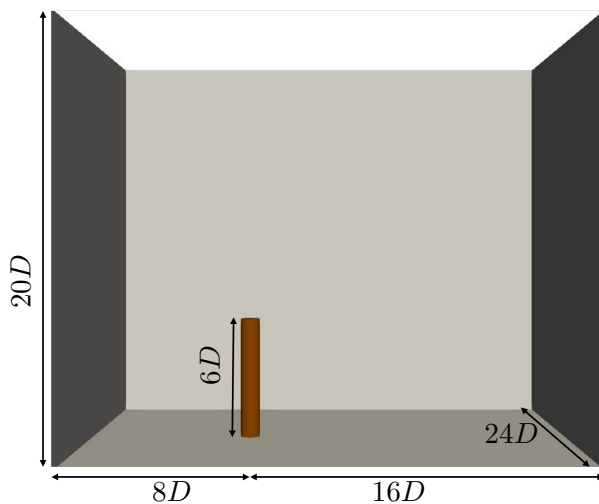

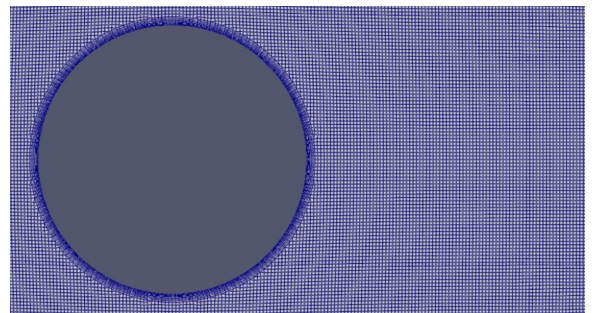Figure 1: Computational domain for the validation case of the cantilever cylinder.

Figure 2: SnappyHexMesh is generated such that first layer is placed inside the viscous sublayer.

2.1.2. Step and infinite cylinder models setup Considering the practical dimensions of an offshore subsea power cable buoyancy section, the ratio of the step cylinder is $D/d = 4$, while the aspect ratio is $L/D = 5$ in the present study. Here, D and d represent the diameter of the LDC and SDC, respectively, while L represents the length of the LDC. The diameter of the large cylinder D is taken as the reference length for analysis. Three different edge features, flat, fillet, and chamfered, are tested for the LDC, resembling different possible buoyancy element shapes. The chamfer angle is 45° with a distance of $\frac{13D}{32}$ away from the junction, while for the fillet, the radius is $\frac{D}{5}$. The diameter of the cylinder for the fillet and chamfer cases is raised to accommodate the loss in volume due to the machining process. The increase in diameter for the LDC is minimal, and the ratio of the diameters remains the same. A uniform inlet velocity condition is applied to the inlet patch.

Most of the numerical settings are similar to the previous validation setup in Section 2.1.1. The numerical tunnel is resized in the lateral and longitudinal direction to $16D$ and $10D$, respectively, resulting in a blockage ratio of 3.5 %. The boundary conditions remain identical to the previous case, with the difference at the bottom patch, which has a symmetry condition instead of a nonslip condition. The flow is simulated for 184 vortex-shedding cycles. Fields are averaged for the last 64 shedding cycles. Two different mesh refinements were considered, one having a coarser mesh with an average y^+ value of 1.5 and the second with an average y^+ value less than 1. Meshes contain 4 million and 24 million cells, respectively.

To simulate the infinite cylinder, the LDC is removed and replaced by the symmetry boundary condition while the rest of the settings remain the same.

3. PANS model validation studies

To ensure the accuracy and reliability of the numerical model, validation studies are carried out for the cantilever and infinite cylinder models in this study.

### 3.1. Cantilever finite cylinder model

Firstly, the PANS model is validated against the wind tunnel experiment conducted by Park and Lee [16] on a cantilever wall-mounted cylinder. Previously, this setup had been validated with Large Eddy Simulation (LES) [17, 18] and PANS by Basara et al. [19]. The results of the surface pressure coefficient profile measured at different heights across the cylinder wall compared to the experimental findings are shown in Figures 3a to 3d. The flow across the cylinder is separated at an angle of $\theta = 76.9°$. Compared to the results from the simulations with $f_k = 0.5$, the PANS simulation with $f_k = 0.1$ resulted in more accurately predicting the surface pressure coefficient distribution across the cylinder at four different heights. The pressure reduction near the free end at $z/D = 0.75$ is due to the fluid movement towards the separation point at the top surface shown in Figure 4. The numerical results yield similar pressure profiles up to the midsection, with a small percentage of error in prediction occurring near the free end. This is the reason for the deviation in the pressure coefficient to the experimental setup. Overall, the results in present settings are comparable to the previous PANS study. A visualization of the mean flow pattern in Figure 4 successfully produced recirculation bubbles at the top surface and the leeward edge of the cylinder, consistent with the prior numerical prediction using four equations near wall PANS model [19]. The generation of vortex near the top edge emphasizes that the downwash effects are dominant in the upper half near the free end of the cylinder. The contours of the Q criterion, also called the second invariant of the velocity gradient tensor, show vortical features across the circular beam similar to the previous findings [17, 18, 19] shown in Figure 5. Frequency analysis of the total side force (lift force) of the entire cylinder resulted in Strouhal numbers of 0.150 and 0.148 for f_k values of 0.1 and 0.5, respectively. These values are close to the experimentally determined Strouhal number of 0.141 [16].
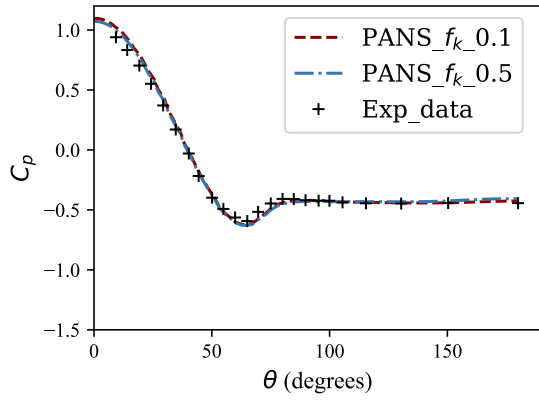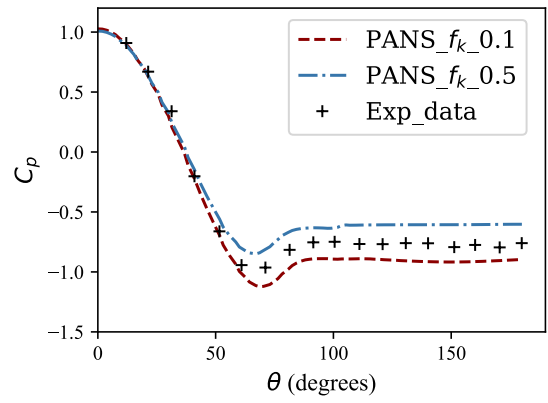
(a) $z/D = 0.3$.
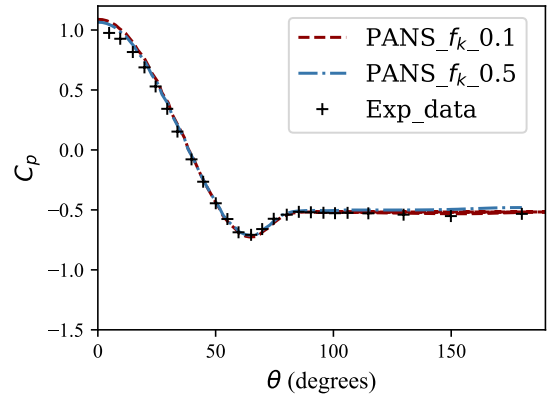
(b) $z/D = 0.5$.
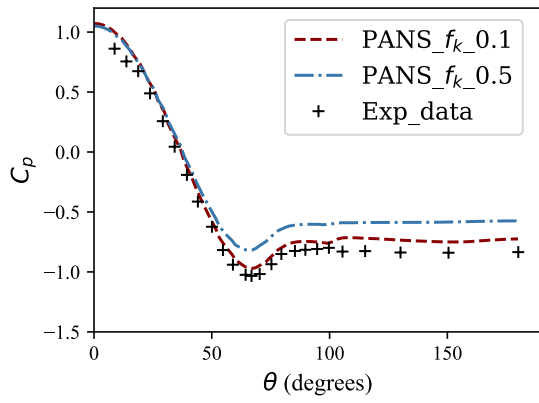
(c) $z/D = 0.75$.

(d) $z/D = 0.917$.

Figure 3: Pressure coefficients at different positions along the cylinder.
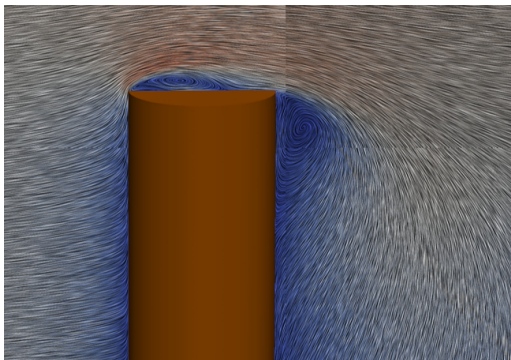

Figure 4: Line integral convolution of the mean velocity at the midsection of the y-plane, colored by mean velocity magnitude.
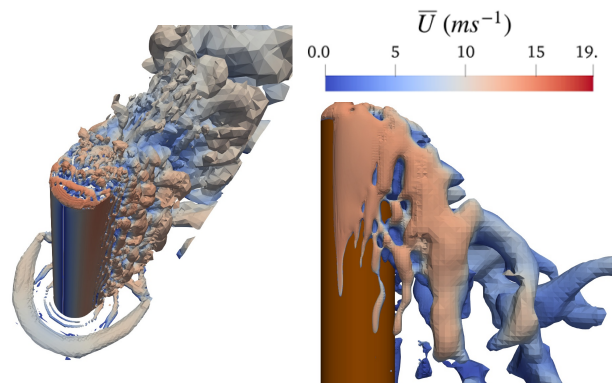

Figure 5: Contours of the Q-criterion (left) and pressure (right) at $Q = 2222\,\text{s}^{-2}$ and $C_p = -0.4$, respectively; color by mean velocity magnitude.

An isolated finite cylinder with a free end is also simulated at Reynolds number 2.5×10^4, and the results yield the drag coefficient of 0.805 consistent with the literature of free end cylinder with dimension $D/L = 5$ at this Reynolds number range [20].

3.2. Infinite cylinder model
For the infinite cylinder, a drag coefficient of 1.16 is obtained, which is close to the experimental value of 1.09 ± 0.5 at a Reynolds number of 6250 [21, 22]. Vortical features represented in Figure 6 are similar to the infinite circular cylinder studies.
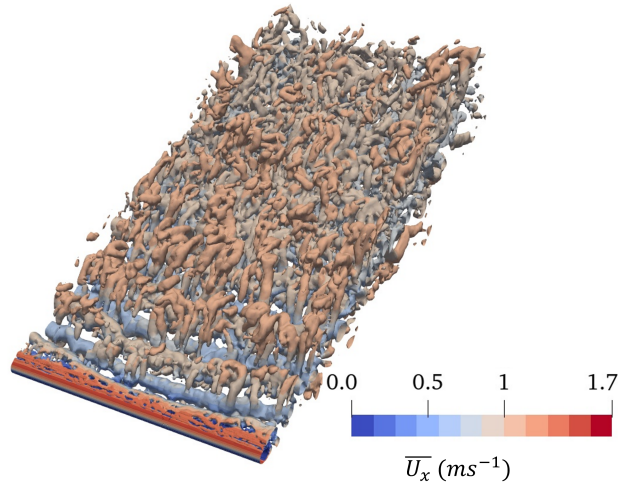

Figure 6: Contours of Q-criterion of the infinite SDC at $Q = 4\,\mathrm{s}^{-2}$; colored by mean velocity magnitude.

4. Results and discussion
The focus of the study is to determine if simplified current practices for estimating forces in subsea power cables can be modified. Therefore, the study examines the flow interaction between step cylinders representing a subsea power cable with buoyancy modules, aiming to identify any changes in the drag force distribution and flow characteristics of the step cylinder. All simulation setups used a factor of $f_k = 0.1$ due to good results obtained for the cantilever cylinder validation case.

4.1. Force distribution
Figure 7 shows the averaged sectional drag coefficient distribution along the infinite cylinder, finite cylinder, and step cylinder with sharp, chamfered, and fillet edges. The obtained averaged drag coefficient for the step cylinder is comparable to a finite and an infinite cylinder with an open end. Overall, a reduction of the drag force on the SDC near the junction for all the step cylinder cases is observed, as shown in Figure 7a. The sectional drag along the SDC decreases at a distance of $2D$ from the interface of the two cylinders, where D represents the diameter of the LDC, as shown in Figure 7a. Moreover, looking along the SDC section for the chamfered case, the drag force is initially higher at a distance of $2D$ and then subsequently becomes lower up to the interface of the two cylinders. Absolute drag coefficient values are adjusted to align with the graph profile to provide a comparison of the change in the drag resulting from the modified edges of the LDC section due to uncertainty in simulations with temporal and spatial discretization for each case. The averaged drag values on the SDC section are 1.15, 1.45, and 1.10

for the sharp, chamfered, and filleted cases, respectively. Filleting causes the most significant overall drag force reduction by 8% on the SDC section after a distance of $2D$ from the interface compared to the chamfered and sharp edges. However, the sharp edge causes a sudden increase in force experienced at the cylinder junction, consistent with previous experimental findings for step cylinders with the setting of $D/d = 2$ [7]. High oscillations occurring near the sharp edge shown in the iso-contour of the Q criterion in Figure 8 might cause the increase of force observed close to the interface for the sharp edge case.
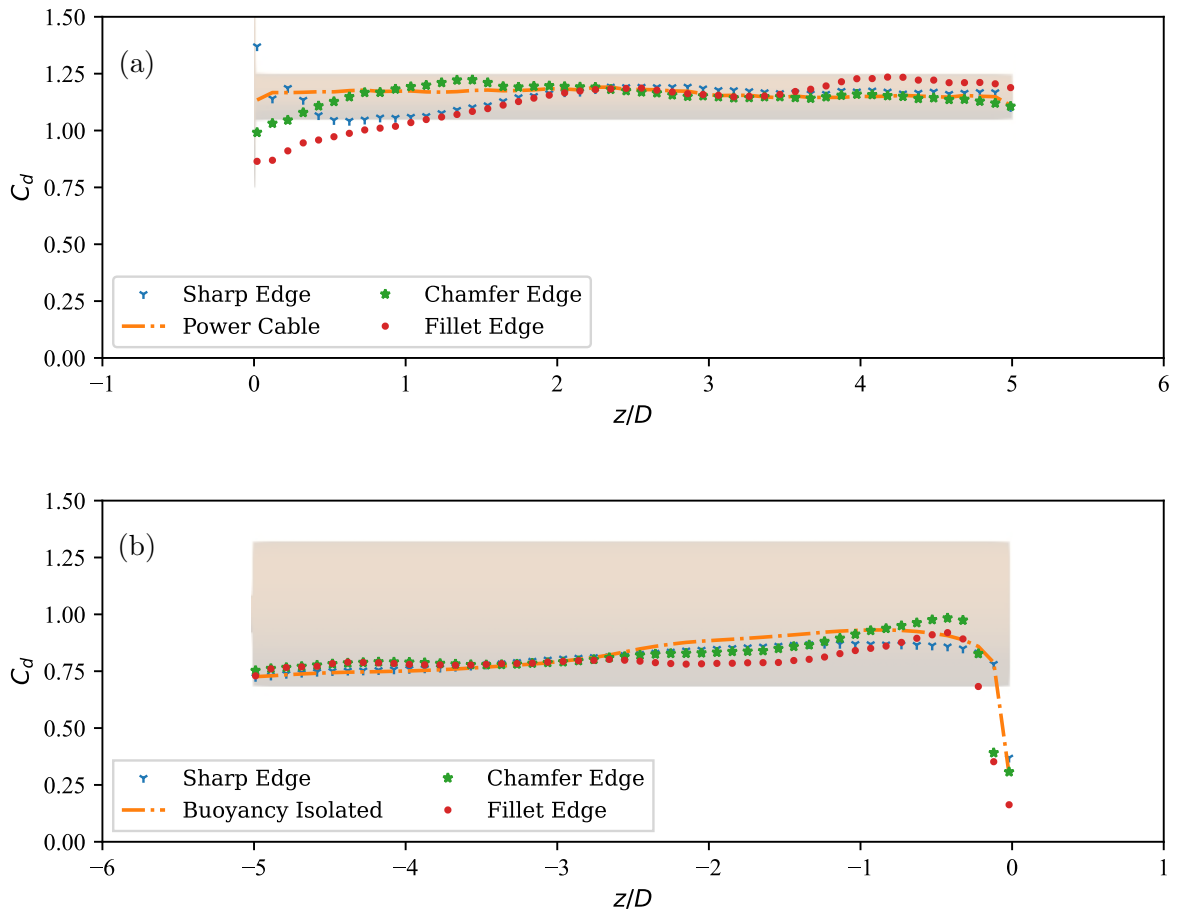

Figure 7: Sectional drag coefficient distribution along the SDC (upper) and LDC (lower).

The drag experienced by the LDC varies at a distance of $2.5D$ to the end of the cylinder junction, as visualized in Figure 7b. However, there is only a slight difference in drag values due to chamfering and filleting, with filleting resulting in the highest overall reduction in drag force by 3.34%. The overall drag coefficients for sharp, chamfered, and fillet cylinders are 0.82, 0.82, and 0.79, respectively. There are two reasons for the sectional drag reduction observed in this case. Firstly, the chamfer and fillet shapes are more streamlined than sharp edges and guide the fluid towards the vortex at the top end of the LDC, which results in a reduction of pressure upstream near the top. Secondly, the chamfered and filleted edges have a reduced surface area, which decreases the drag coefficient.

4.2. Flow patterns

The flow observed is unsteady and three-dimensional. However, 2-D plane cuts are performed for better understanding. Velocity contours for the cross-section of the step cylinders with sharp, chamfered, and filleted edge configurations are depicted at three different distances in Figures 9 and 10. In Figure 9, flow separation occurs near the proximity of the sharp edge, leading to a pronounced thick region of recirculated flow upstream of the SDC at position $z = 0.01D$. However, higher positive streamwise velocity is observed upstream due to the absence of flow separation when the edges are chamfer and fillet. Only a small separation occurs at the end of the filleted and chamfered edges just upstream of the SDC due to their streamlined shape, which delays the flow separation. This flow separation phenomenon with the edges is similar to the other studies of bluff body aerodynamics [23].
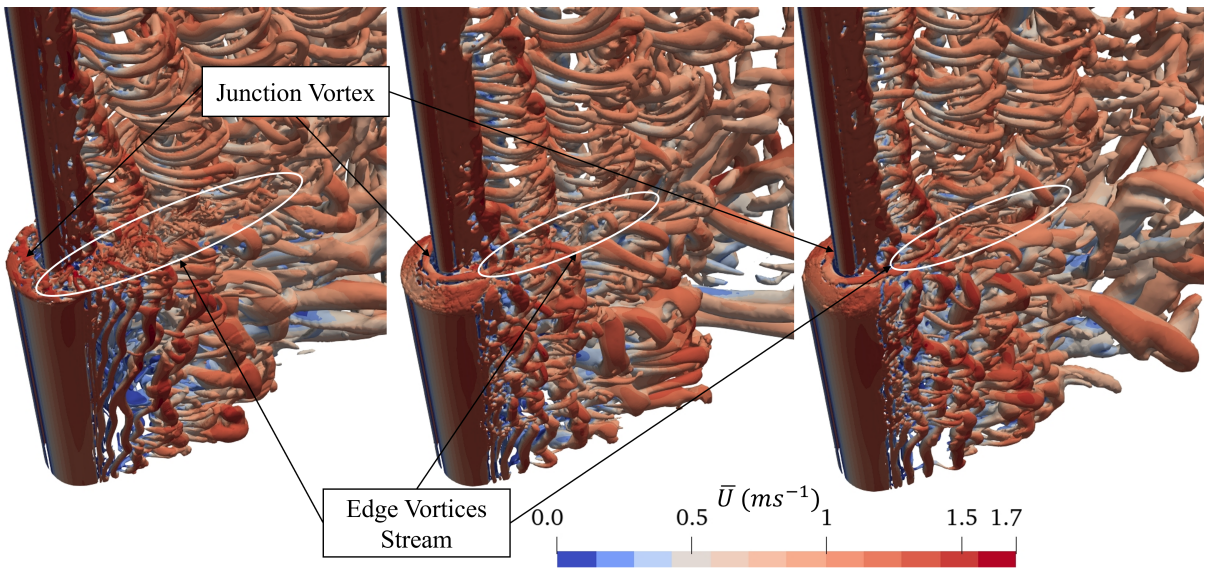

Figure 8: Isocontour of Q-criterion of the step cylinders with sharp (left), chamfered (middle), and fillet (right) edges at $Q = 4\,\mathrm{s}^{-2}$.

The comparison of velocity contours at the mid-section of the step cylinder and the single isolated cylinder cases is shown in Figures 11 and 12. The flow patterns in the wake and junction areas differ for the step cylinder shown in Figure 11 in comparison to the single isolated cylinder depicted in Figure 12. This disparity arises from the interactions between flow fields of SDC and LDC. The velocity contours downstream of the junction for the sharp edge case show accelerated flow and an absence of a substantial reverse flow regime downstream, as depicted in Figures 10 and 11. Conversely, reverse flow is evident for chamfered and filleted edges in these proximity areas. However, the sharp edge configuration leads to a downward flow and the formation of a sizable recirculation region downstream of the LDC shown in Figure 11. Reduction in the size of this recirculation region in the downwash region is seen in the results of chamfers and filleted edges.

The merging of two cylinders generates a distinct and complex coherent flow pattern, as shown in Figure 8. This pattern differs significantly from what was observed with an isolated cylinder case in Figure 6. The presence of a SDC as an obstruction induces the formation of vortices at the rear of the cylinder. The vortices generated from the SDC are pushed slightly downward due to a higher negative pressure region downstream. Notably, streams of edge vortices are visible for configurations with sharp edges similar to the tip vortices seen at the wingtips of an aircraft [24].

However, these vortex streams are less pronounced in cases where the edge of the LDC features a fillet or chamfer. This discrepancy emerges because of the pressure difference created between the top surface and sides of the cylinder. In the case of a sharp-edged cylinder, the thicker junction vortex upstream elucidates the pronounced reverse flow in the velocity contour plot depicted in Figure 9. On the contrary, in the fillet and chamfer cases, a thinner junction vortex
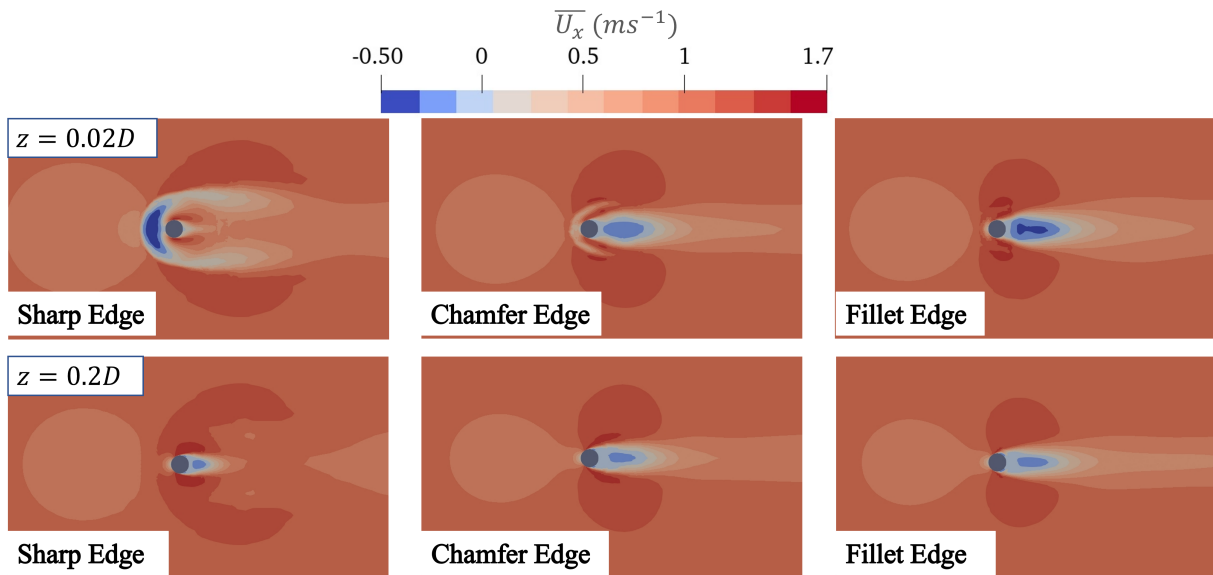

Figure 9: 2-D streamwise velocity contours for the three step cylinder cases at two different cross-sectional positions: $z = 0.02D$ and $z = 0.2D$ (arranged vertically) from the step cylinder junction along the SDC.
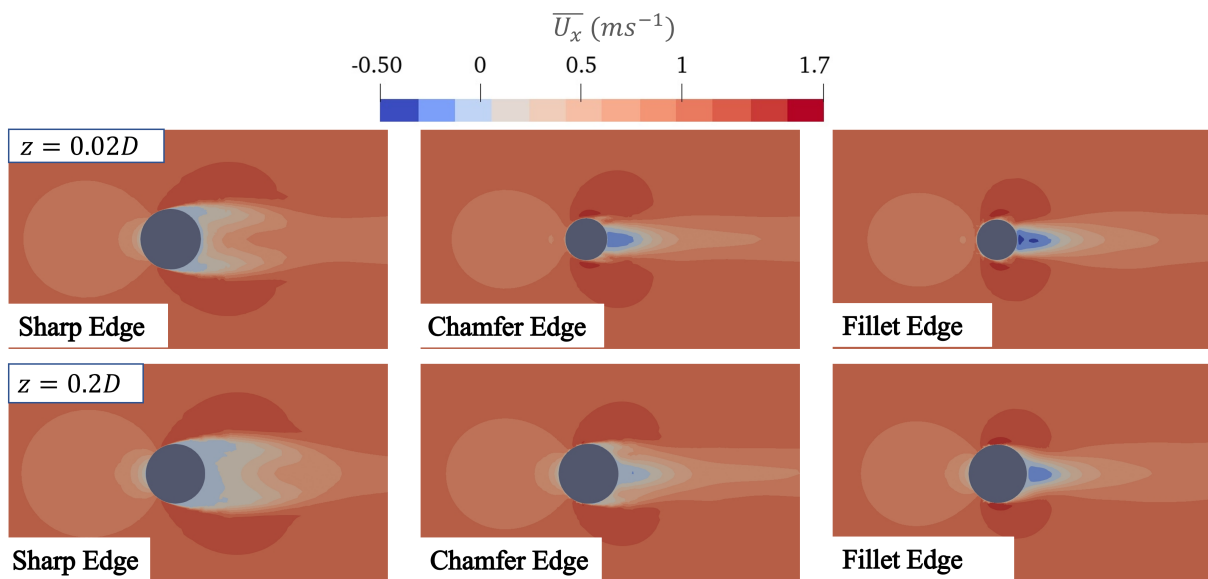

Figure 10: 2-D streamwise velocity contours for the three-step cylinder cases at two different cross-sectional positions: $z = 0.02D$, and $z = 0.2D$ from the junction of the step cylinder along the LDC.
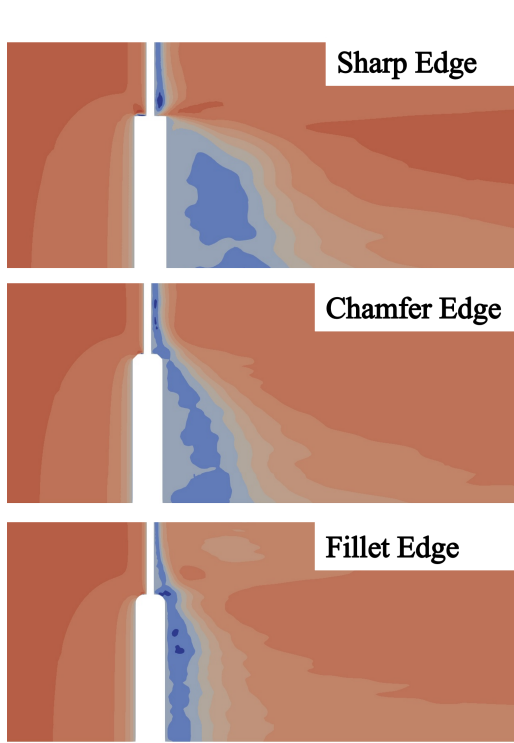
Figure 11: Streamwise velocity contours for the three different step cylinder cases at mid-section: sharp, chamfer, and fillet.
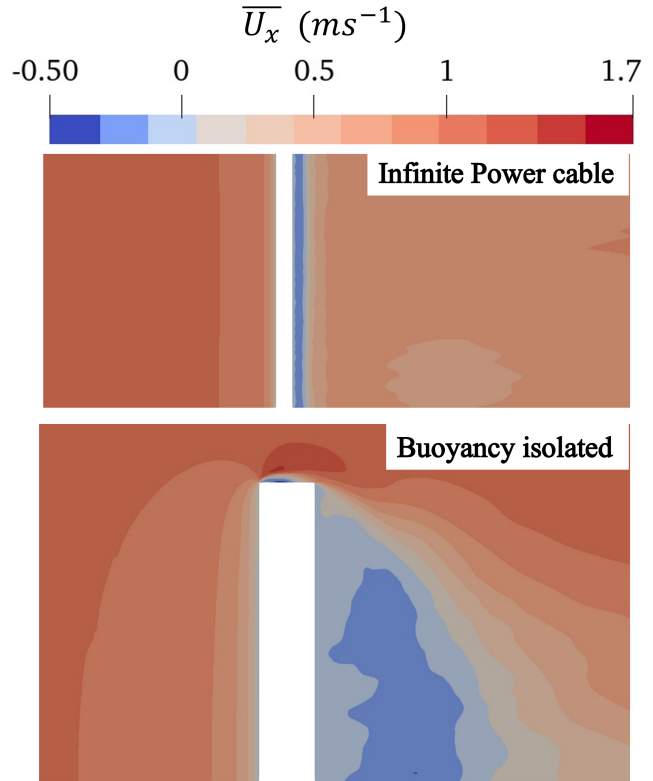

Figure 12: Streamwise velocity contours for the infinite power cable cylinder (top) and the sharp edged isolated buoyancy element finite cylinder (bottom) cases at the midsection.

in the form of a horseshoe is generated.

5. Conclusions

This study applied the PANS method to investigate flow structures and excitation forces on step cylinder configurations with a larger-to-smaller diameter ratio of $D/d = 4$. A comparative analysis to assess the influence on the flow of different edge shapes, namely sharp, fillet, and chamfer, on the LDC was carried out.

A validation study was performed on the cantilever wall-mounted cylinder, and pressure results obtained at the various heights of the cantilever wall-mounted cylinder closely matched experimental results. PANS simulations with the resolved-to-unresolved turbulence ratio $f_k = 0.1$ yielded more accurate results than when using $f_k = 0.5$. Hence, the step cylinder simulation was conducted using $f_k = 0.1$. The results are examined for sectional drag forces, velocity distribution contours, and vortical flow structures.

These are the findings for the step cylinder cases:

- The overall drag coefficient obtained on SDC and LDC is 1.15 and 0.82, respectively. Simulations show that the drag force on the SDC decreases at a distance $2D$ from the cylinder junction. Fillet edge case results in an overall sectional drag force reduction of 8% and 3.5% on the SDC and LDC, respectively, compared to the sharp edge case.

- On the top surface of the sharp cylinder, upstream of the interface, a wider reverse flow regime is observed as compared to the fillet and chamfer cylinders. Moreover, when the

sharp edge is converted to a chamfer and a fillet edge, it causes a reduction in the size of the recirculation region behind the LDC.

- For all step cylinder cases, a junction vortex is formed at the top surface of the LDC. Upstream of the SDC, the large recirculating junction vortex is formed at the sharp edge of the LDC, with a stream of edge vortices on the sides. However, chamfering and filleting the edge reduces the junction vortex size and minimizes the edge vortices intensity.

The DNV-RP-C205 practice estimates the transverse drag coefficient for riser sections with buoyancy elements by adjusting a two-dimensional drag coefficient for finite length effects. For the present study, the reduction factor is 0.68 for the buoyancy module represented by a LDC with a length-to-diameter ratio of 10, including the symmetry condition. With a drag coefficient of 1.2 for infinitely long smooth cylinders in the subcritical regime, the resulting buoyancy module drag coefficient is 0.82. This value is higher than those obtained for the LDC with a fillet edge. However, a drag coefficient of 1.2 is usually assumed for power cables, considering an infinitely long smooth cylinder in the subcritical regime. This value does not account for the decrease in the drag coefficient over a length of $2D$ from the buoyancy module observed in the present study.

In future research, it would be valuable to investigate the effects of varying diameter ratios of the different cylinders. If the distance between two buoyancy elements is less than $2D$, the drag coefficient will be different than in the present study since the step cylinder influences the drag on the power cable up to this length. Double-step cylinder simulations with a SDC in between with a length of $2D$ should be carried out, as the flow from the two LDCs will interact, influencing the drag. Due to the complex vortical interactions observed at the junction, a detailed analysis of the effects of vortex-induced vibrations can be conducted. Moreover, the impact of varying inlet current speed and inclination angle on flow should be evaluated for further studies.

References
[1] DNV AS 2021 Environmental conditions and environmental loads Recommended Practice DNV-RP-C205 Det Norske Veritas
[2] Huse E and Reitan O E 1989 Drag of Buoyancy Elements on Flexible Risers in Axial Flow Tech. Rep. 511171.00-1 MT51 89-0198 MARINTEK Trondheim, Norway
[3] Schnepf A, Lopez-Pavon C, Ong M C, Yin G and Johnsen Ø 2023 Feasibility study on suspended inter-array power cables between two spar-type offshore wind turbines *Ocean Eng.* **277** 114215 ISSN 00298018
[4] Chua L P, Liu C Y and Chan W K 1998 Measurements of a step cylinder *Int. Commun. Heat Mass Transf.* **25** 205–15
[5] Dunn W and Tavoularis S 2006 Experimental studies of vortices shed from cylinders with a step-change in diameter *J. Fluid Mech.* **555** 409–37
[6] Morton C, Yarusevych S and Carvajal-Mariscal I 2009 Study of flow over a step cylinder *Appl. Mech. Mater.* **15** 9–14
[7] Ko N W M and Chan A S K 1990 In the intermixing region behind circular cylinders with stepwise change of the diameter *Exp. Fluids* **9** 213–21
[8] Zdravkovich M and Bearman P 1998 *Flow around circular cylinders—Volume 1: Fundamentals* (Cambridge University Press)
[9] AS P 2023 Offshore & Subsea - Buoyancy systemes and cable protection solutions
[10] Girimaji S S 2005 Partially-Averaged Navier-Stokes Model for Turbulence: A Reynolds-Averaged Navier-Stokes to Direct Numerical Simulation Bridging Method *J. Appl. Mech.* **73** 413–21 ISSN 0021-8936
[11] Menter F R 1992 Improved two-equation k-omega turbulence models for aerodynamic flows Tech. rep. National Aeronautics and Space Administration Ames Research Center
[12] Girimaji S S and Abdol-Hamid K 2005 Partially-averaged navier stokes model for turbulence: Implementation and validation *43rd AIAA Aerospace Sciences Meeting and Exhibit* p 502

[13] Elmiligui A, Abdol-Hamid K, Massey S and Pao S 2004 Numerical study of flow past a circular cylinder using rans, hybrid rans/les and pans formulations *22nd Applied aerodynamics conference and exhibit* p 4959

[14] Davidson L and Friess C 2019 A new formulation of fk for the pans model *J. Turbul.* **20** 322–36

[15] Klapwijk M, Lloyd T and Vaz G 2019 On the accuracy of partially-averaged navier–stokes resolution estimates *Int. J. Heat Fluid Flow* **80** 108484

[16] Park C W and Lee S J 2002 Flow structure around a finite circular cylinder embedded in various atmospheric boundary layers *Fluid Dyn Res* **30** 197

[17] Afgan I, Moulinec C, Prosser R and Laurence D 2007 Large eddy simulation of turbulent flow for wall mounted cantilever cylinders of aspect ratio 6 and 10 *Int. J. Heat Fluid Flow.* **28** 561–74

[18] Krajnović S 2011 Flow around a tall finite cylinder explored by large eddy simulation *J. Fluid Mech.* **676** 294–317

[19] Basara B, Krajnovic S, Girimaji S S and Pavlovic Z 2011 Near-wall formulation of the partially-averaged navier stokes turbulence model *AIAA J.* **49** 2627–36

[20] Cengel Y and Cimbala J 2013 *Ebook: Fluid mechanics fundamentals and applications (si units)* (McGraw Hill)

[21] Clift R, Grace J R and Weber M E 2005 *Bubbles, drops, and particles* (Dover Publications)

[22] Wieselsberger C 1922 New data on the laws of fluid resistance Tech. rep. Aerodynamic Institute, Gottingen

[23] Yaghoubi M and Mahmoodi S 2004 Experimental study of turbulent separated and reattached flow over a finite blunt plate *Exp. Therm. Fluid Sci.* **29** 105–112

[24] Anderson J 2011 *EBOOK: Fundamentals of Aerodynamics (SI units)* (McGraw hill)